Title
Glial cells influence cardiac permittivity as evidenced through in vitro and in silico models

Journal
Biofabrication, 12(1)

ISSN
1758-5082

Authors
Soucy, Jonathan R
Askaryan, Jody
Diaz, David
et al.

Publication Date
2020

DOI
10.1088/1758-5090/ab4c0a

Peer reviewed

Glial cells influence cardiac permittivity as evidenced through in vitro and in silico models

Glial cells influence cardiac permittivity as evidenced through in vitro and in silico models

Jonathan R. Soucy, Jody Askaryan, David Diaz, Abigail N. Koppes, Nasim Annabi, Ryan A. Koppes

Keywords: Tissue Engineering, electrophysiology, Heart, Gap Junctions, Computational Modeling, I*n Vitro* Modeling, Microphysiological systems; GelMA; Schwann cells; Cardiomyocytes; organs-on-chip; excitation-contraction coupling

Abstract

Excitation-contraction (EC) coupling in the heart has, until recently, been solely accredited to cardiomyocytes. The inherent complexities of the heart make it difficult to examine non-muscle contributions to contraction *in vivo,* and conventional *in vitro* models fail to capture multiple features and cellular heterogeneity of the myocardium. Here, we report on the development of a 3D cardiac μTissue to investigate changes in the cellular composition of native myocardium *in vitro*. Cells are encapsulated within micropatterned gelatin-based hydrogels formed via visible light photocrosslinking. This system enables spatial control of the microarchitecture, perturbation of the cellular composition, and functional measures of EC coupling via video microscopy and a custom algorithm to quantify beat frequency and degree of coordination. To demonstrate the robustness of these tools and evaluate the impact of altered cell population densities on cardiac μTissues, contractility and cell morphology were assessed with the inclusion of exogenous non-myelinating Schwann cells (SCs). Results demonstrate that the addition of exogenous SCs alter cardiomyocyte EC, profoundly inhibiting the response to electrical pacing. Computational modeling of connexin-mediated coupling suggests that SCs impact cardiomyocyte resting

potential and rectification following depolarization. Cardiac μTissues hold potential for examining the role of cellular heterogeneity in heart health, pathologies, and cellular therapies.

Ischemic heart disease remains a leading cause of death worldwide. While pharmacological interventions have improved life expectancy by mitigating key risk factors, therapeutic strategies for repairing the damaged myocardium have yet to become the clinical standard (Björnson et al., 2016; Hashimoto et al., 2018). Following infarct, delivery of autologous cells, including mesenchymal stem cells, cardiac stem cells, and endothelial progenitor cells, have yielded promising results at the benchtop, but inconsistent benefits in clinical trials (Hatzistergos and Vedenko, 2017; Malliaras and Marbán, 2011; Muller et al., 2018; Tang et al., 2018). To improve the efficacy of potential therapeutic strategies, new experimental models at the benchtop that enhance our fundamental understanding of the contribution of cardiac support cells are required.

In a healthy heart, cardiomyocytes (CMs) are the most abundant cells by volume, but only make up 25-35% of the total myocardial cells (Pawlak et al., 2018; Perbellini et al., 2018; Pinto et al., 2016; Skelly et al., 2018; Zhou and Pu, 2016). While the percentage of CMs in the heart is relatively accepted, there is a lack of consensus regarding the interstitial cell composition in the heart (Pinto et al., 2016). Current perspectives suggest the presence of fibroblasts, endothelial cells, smooth muscle cells, pericytes, Schwann cells (SCs), macrophages, telocytes stem cells, conduction cells (pacemaker cells and Purkinje fibers), neurons, and atrial and ventricular CMs (Armour, 1991; Gherghiceanu and Popescu, 2012; Nandi and Mishra, 2015; Pawlak et al., 2018; Perbellini et al., 2018; Pinto et al., 2016; Popescu et al., 2015; Skelly et al., 2018; Xin et al., 2013; Zhou and Pu, 2016). Further, the role of electric-coupling of resident, non-myocyte cells such as fibroblasts (Sachse et al., 2008), macrophages (Hulsmans et al., 2017), telocytes (Sheng et al., 2014), and stem cells (Mayourian et al., 2016) has only recently been observed and modeled. Due to current experimental limitations, the investigation of these cell types and their interactions

require a combination of *in vivo*, *in vitro, and in silico* examination. Not only is the composition of the heart diverse, but an accurate understanding of cellular interactions is critical to fully comprehend cardiac pathogenesis and aid the development of new therapeutic strategies (Iseoka et al., 2018; Pinto et al., 2016; Zamani et al., 2018).

The development of robust and biomimetic *in vitro* models recapitulating key features of mesoscale architecture and heterogeneity of *in vivo* counterparts is essential for the study of fundamental biological processes. While traditional two-dimensional (2D) cell culture techniques have been used for decades and contributed greatly to the understanding of cardiomyocyte function, limitations such as atypical cell size and morphology, de-differentiation, and limited cell-cell contacts limit discovery (Natarajan et al., 2011; Zuppinger, 2016). Three-dimensional (3D) cell culture has helped to overcome some of these limitations by providing more physiologically relevant microenvironments, imparting robust mechanical cues as well as intra- and extra-cellular adhesion complexes similar to native tissue (Li et al., 2012; Ravi et al., 2015; Zuppinger, 2019). In typical 3D culture, cells are encapsulated within extracellular matrix (ECM) like materials to more closely mimic the *in vivo* tissue architecture (Gonzalez-Diaz and Varghese, 2016; Tibbitt and Anseth, 2009). However, current 3D culture models are often limited to simple geometries or require the use of complex and expensive microfabrication techniques or microfluidics to form more complex biomimetic 3D constructs. Cell printing has enabled the production of complex 3D structures *in vitro* (Mandrycky et al., 2016), however, the shear forces that cell experience during processing have greatly precluded the use of sensitive cell types like CMs (Kacarevic et al., 2018; Mitcheson et al., 1998).

Photocrosslinkable hydrogels facilitate an alternative to 3D printing by patterning complex shapes and structures to recapitulate *in vivo* architecture of tissues including the heart (DeForest et al., 2009; Yue et al., 2015). However, the reliance on ultraviolet (UV) light in these systems may lead to reduced cell viability (Naseer et al., 2017; Noshadi et al., 2017a). Further, while photocrosslinkable materials are relatively inexpensive to synthesize, the specialized light sources required to polymerize the materials are prohibitively expensive for widespread use. More specifically, there are no *in vitro* models to investigate the impact of resident non-CM cells on cardiomyocyte function. Therefore, there remains a need to develop an alternative inexpensive approach for designing an *in vitro* 3D culture model that can be scaled to systematically examine the multicellular nature of the cardiovascular system.

To address these challenges, here, we describe the development of a biomimetic, 3D *in vitro* model (or cardiac μTissue) to examine the role of different cell types in the heart. Specially, primary cardiac cells were encapsulated at different ratios and variable geometries to assess the importance and function of SCs and the potential influence on local alignment. Previously, the role of SCs in the myocardium has remained difficult to assess *in vivo* as knock-out models are unviable due to abnormal cardiac development during embryogenesis (Barik et al., 2016; Lee et al., 1995; Morris et al., 1999). Therefore, to better mimic the cardiac microenvironment and maintain CM phenotype *in vitro* (Saini et al., 2015; Wanjare and Huang, 2017), a photolithography technique was used to create cardiac μTissues of micropatterned gelatin methacrylate (GelMA) via an inexpensive visible light LED (405 nm) system. Cardiac μTissue functional output was evaluated on a cell-by-cell basis using a novel algorithm to measure beats per minute (BPM) as well as the degree of coordination (DoC). In addition, functional differences between visible and traditional UV light

photocrosslinking systems for encapsulation were compared in patterned and unpatterned systems. As a proof of concept for the potential of these cardiac μTissues to study cardiovascular health and repair, the role of exogenous SC incorporation, an abundant cell type whose function in the heart remains unknown, was characterized (**Fig. 1A**). Lastly, a computational model of SC-CM coupling was developed to provide deeper insight into the underlying SC impact on CM electrophysiology.

Experimental Procedures

2.1 GelMA synthesis and hydrogel fabrication. GelMA, derived from fish gelatin, was synthesized as previously reported(Nichol et al., 2010). In brief, 8% (v/v) methacrylic anhydride (Sigma) was added to a 10% (w/v) fish gelatin (Sigma) solution in Dulbecco's Phosphate Buffered Saline (DPBS, Sigma). The product of this reaction was dialyzed (Spectra/Por 12-14kD, Fisher Scientific) using distilled water for 1 week, and then lyophilized for use on demand. GelMA hydrogel precursor solutions (7.5% (w/v)) were prepared in complete culture medium [Dulbecco's Modified Eagle Medium (DMEM) without phenol red (Sigma) supplemented with 10% fetal bovine serum (Sigma), 2 mM L-glutamine (Gibco), and 50 units/mL penicillin/streptomycin (Gibco)] with 0.5% (w/v) 2-hydroxy-1-(4-(hydroxyethoxy) phenyl)-2-methyl-1-propanone (Irgacure® 2959, CIBA Chemicals) or 0.5% lithium phenyl-2,4,6-trimethylbenzoylphosphinate (LAP, Biobots) as photoinitiators. Hydrogel precursors were then photocrosslinked by exposure to UV light (365 nm) with an Omnicure S2000 (Excelitas Technologies) for Irgacure® containing precursor hydrogels or visible light (405 nm) with a 10W LED (QUANS) for LAP containing precursor hydrogels (0.25 seconds of 10 mW/cm^2 light exposure per μm of hydrogel thickness).

2.2 Mechanical characterization. The compressive modulus of each hydrogel formulation (5%, 10%, and 15% (w/v) polymer concentration for UV and visible light crosslinked hydrogels) was examined using an ElectroForce mechanical load frame (TA instruments) with a 1000 gr load cell. Hydrogel samples were prepared in custom polydimethylsiloxane (Sylgard) molds (cylinders of 6 mm diameter; 4 mm height). Hydrogels were loaded between two compression platens, and cyclic uniaxial compression tests were conducted at 0.5 Hz (10 cycles). Compression displacement and load for each cycle were recorded using WinTest7 software. The compressive modulus was calculated as the tangent slope of the linear region of the stress-strain curves between 0.1 – 0.25 stain level. Three independently prepared samples for each formulation were measured to quantify the compressive modulus.

2.3 Primary cardiac cell isolation. Primary CMs and adherent cardiac cells (aCCs) were isolated from two-day old (p2) Sprague-Dawley neonatal rat (Charles River) hearts, following a modified protocol by Noshadi *et al.* (Noshadi et al., 2017b) and approved by Northeastern's Institutional Animal Care and Use Committee (IACUC). In brief, the thorax was opened and the heart was removed. The major veins and atria were then removed so that only the left and right ventricles remained. The ventricles were cut into 3-4 pieces and stored in 0.05% (v/v) trypsin (Gibco) in Hank's balanced salt solution (HBSS, Gibco) at 4 °C with continuous shaking overnight. The following day, the ventricle pieces were removed from the trypsin and subject to sequential collagenase treatments (305 units Collagenase II (Gibco) in HBSS) at 37 °C to dissociate the connective tissue and collect cardiac cells. Cells were then filtered through a 70-µm cell strainer (Falcon) and pre-plated in a tissue culture flask (T-175, Corning) with complete culture medium to enrich the CM population by differential adhesion. After one hour in standard cell culture

conditions (37 °C, 5% CO_2), any unattached cells were considered to be CMs, while those attached cells were deemed aCCs. Each cell population was then counted and used for experimentation within one hour following completion of the pre-plating enrichment.

2.4 SCs isolation. Primary SCs were isolated from p2 Sprague-Dawley neonatal rat sciatic nerves using established protocols (Koppes et al., 2014; Soucy et al., 2018). Sciatic nerves were harvested and kept in complete culture medium on ice for a maximum of 4 h. Dissected nerves were minced into 1-2 mm pieces under sterile conditions and incubated in a 6-well plate using complete culture medium in standard conditions. Tissue were then transferred to a new dish after visual confirmation of fibroblast migration. Three to four days after SC migration, cells were cultured with complete medium supplemented with 10^{-5} M cytosine arabinoside (Sigma) for 72 h to remove remaining highly mitotic fibroblasts. Next, a complement-mediated cell lysis was used to eliminate remaining fibroblasts. Cells were detached with 0.25% (v/v) trypsin/EDTA (Corning) and pelleted at 200 g for 5 min. Fibroblasts were targeted by re-suspending in 1 mL anti-CD90/Thy 1.1 (diluted 1:500 v/v in DMEM, Cedar Lane Labs) and incubated under standard conditions for 30 min. Treated cells were pelleted, re-suspended in 1 mL rabbit complement, and incubated for 30 min with standard conditions to selectively lyse the fibroblasts. After incubation, cells were centrifuged, re-suspended in SC maintenance medium (complete medium supplemented with 6.6 mM forskolin (Sigma) and 10 µg mL^{-1} bovine pituitary extract (Corning)), and cultured in a flask for expansion. Lysis was repeated if fibroblast impurities remained. SC purity was assessed using anti S-100 (DAKO). Maintenance medium was changed every other day and SCs were passaged before 100% confluency until P10.

2.5 3D cell encapsulation. Equal parts of enriched CMs and aCCs (1:1), or CMs, aCCs, and SCs (1:1:1), were mixed with the hydrogel precursor solution (7.5% GelMA (w/v) and 0.5% (w/v) Irgacure® or LAP) at a density of $1.5x10^7$ cells/mL. Approximately 10 μL cell-laden gel precursor solution was placed between a 180 μm-tall spacer and a 3-(trimethoxysilyl) propyl methacrylate (ACROS Organics) coated glass slide, followed by 45 seconds ($10mW/cm^2$) light exposure through a laser cut black cardstock paper photomask (500 μm lines) to form patterned cell-laden hydrogels. Samples were incubated for 10 days in standard culture conditions with medium replaced every other day. Cell viability within 3D cardiac μTissues was determined via a LIVE/DEAD® viability/cytotoxicity kit (Life Technologies) one day post encapsulation.

2.7 Cardiac beating quantification. Individual CM contractions within the 3D μTissues were quantified with a custom MATLAB (Mathworks) code to calculate beats per minute (BPM) on a cell-by-cell basis using video microscopy. Cardiac cells were recorded at 30 frames per second with phase contrast on a Zeiss Axio Observer at 20x with an incubation chamber (37°C and 5% CO_2). Raw video files were exported as AVIs (M-JPEG compression, 90% quality) and imported into MATLAB for analysis. Regions of interest (ROIs) were identified from the first frame of the video recording as objects between 75 μm^2 – 1000 μm^2 in size (**Figure S1A**). To quantify BPM, the sum differences in frame-to-frame pixel intensity were measured for each ROI. Inclusion criteria for a beating CM was: 1) peak amplitude was greater than one standard deviation above the mean, 2) negative spikes were less than two standard deviations below the mean, and 3) the frequency of spikes was below 6 Hz (**Figure S1B-C**). After passing these prerequisites, beating was recorded as the number of spikes found in inclusion criteria 1. However, for high frame rate movies (frames per second > 10), both CM contraction and relaxation may result in recorded spikes

(**Figure S1D**). To record only a single beat per contraction, the mean inter-spike-interval was calculated for each cell and spikes occurring below this value were disregarded. The average BPM was then calculated as the mean number of contractions for all ROIs in field of view ($m > 20$) multiplied by 60 and divided by the video length from a minimum of three samples per condition ($n > 3$).

To validate of accuracy and precision of this algorithm for measuring CM beating, simultaneous video microscopy (Axio Examiner at 40x) and electrical potential via a multielectrode array (MEA, multichannel systems) recordings were acquired and compared. Timestamps for each contraction from the identified CMs were assigned a unique identification number to gather a quantification on the degree of coordinated contraction in the μTissue models. Specifically, timestamped contraction data was imported into a modified algorithm originally developed to investigate neuronal activity (Kreuz et al., 2015), and values of one minus the SPIKE-distance, an estimator of the similarity between spike trains, were reported as a means to quantify degree of coordinated CM contractions.

2.8 External electrical pacing. Electrical pacing of CMs was assessed using a chamber designed to apply pulsatile electrical stimuli(Tandon et al., 2009) (50% duty square waves) to patterned cell-laden hydrogels at increasing frequencies (0.5, 1, 2, and 3 Hz) and voltage (1, 3, and 5 V) for 30 s. Alternating electrical stimulation was applied via two carbon rod electrodes mounted in a glass petri dish 2 cm apart. Pulsatile electrical signals were applied using a function generator (Agilent) connected to each carbon electrode with platinum wires. Alternating current stimulation was implemented to minimize hydrolysis. The chamber was filled with complete medium and each

cell-laden hydrogel μTissue was aligned along the axis of the applied electric field between the two electrodes. The battery of conditions was randomized across samples to negate influence of testing order, and a minimum of five samples were examined at all frequencies and voltages.

2.9 Immunocytochemistry. Cell-laden μTissues were fixed with 4% paraformaldehyde (30 min), permeabilized with 0.1% X-100 Triton (20 min), then blocked with 5% goat serum (>12 h) in DPBS. After overnight blocking, samples were incubated in 1:400 rabbit anti S-100 (DAKO, Z0311), 1:200 mouse anti sarcomeric α-actinin (Abcam, ab9465), mouse anti CD90, and/or 1:200 goat anti connexin-43 (Abcam, ab87645) in blocking solution overnight at 4 ºC. Cell-laden hydrogels were then washed thrice with DPBS and anti-rabbit, anti-mouse, and anti-goat secondary antibodies (1:200 in goat serum) were added overnight at 4 ºC. Samples were rinsed with DPBS and mounted on cover slides with ProLong® Gold Antifade with 4',6-diamidino-2-phenylindole (DAPI). Lastly, the constructs were imaged using an inverted fluorescence microscope (Zeiss Axio Observer Z1).

2.10 Computational model of SC-CM Coupling. SC electrophysiological properties were mathematically simulated by curve fitting published voltage clamp data to a Hodgkin-Huxley model using MATLAB. Specifically, type I potassium (Baker and Ritchie, 1996), L-type calcium (Amédée et al., 1991), and the sodium currents (Howe and Ritchie, 1990) were incorporated into this model. The electrophysiology properties of a beating cardiomyocyte coupled to a SC was modeled as previously described (Sachse et al., 2008). Model parameters are expanded upon in Supplementary Information.

2.11 *Statistical analysis.* All data was first determined to be normally distributed using the Lilliefors test in MATLAB. Normally distributed data was compared in MATLAB by using a student-t test for data sets containing only two experimental conditions (**Figure 6D**), a one-way ANOVA for experiments with more than two conditions (**Figures 1C, 2E, 4C, and 6A-B**), and a multi-way ANOVA for comparisons across multiple days (**Figures 3 and Fig. 5A-B**). Non-normally distributed data was compared in MATLAB with the Kruskal-Wallis test (**Figure 5G**). A minimum of three images from three independent samples were analyzed to quantify viability, aspect ratio, and total cell percentage. Error bars represent the mean ± standard deviation of measurements (**$p < 0.05$).

Results

Cardiac Tissue Models

3D cardiac cultures were developed to rapidly and inexpensively synthesize μTissues. GelMA hydrogels were crosslinked with either a UV or visible light photoinitiator system: Irgacure® using an Omnicure S2000 (365 nm) or LAP using a custom 405nm LED system (**Figure S2A**). The compressive modulus of the visible crosslinked hydrogels increased significantly from 1.16 ± 0.04 kPa for 5% (w/v) GelMA to 22.56 ± 1.91 kPa for 10% GelMA to 80.49 ± 2.75 kPa for 15% GelMA (**Figure S2B**). Based on these data, a 7.5% (w/v) GelMA hydrogel was selected to best mimic the stiffness of the native cardiac tissue (mean 6.8 kPa) (Bhana et al., 2010).

Primary cardiac cells were encapsulated in patterned (500 μm wide lines; 2 mm separation) GelMA hydrogels by controlling the areas of the precursor hydrogel that were exposed to light

using laser cut black cardstock paper (**Figure 1B**). 3D μTissues exhibited increased viability (93.44 ± 3.75) compared to constructs formed with UV light, irrespective of the photoinitiator (**Figures 1C and S3**). This method was used to fabricate a range of 3D geometries conventionally only achievable using microfluidics or bioprinting (**Figure 1D**). Further, by adjusting the height of spacers from 180 μm to 360 or 540 μm, we demonstrated the ability to form a range of μTissue thicknesses as well as assembling layers of different compositions (**Figure 1E**). However, despite our ability to increase μTissue thickness, a nutrient diffusion limitation would exist for hydrogels > 300 μm that may significantly decrease CM viability (Figueiredo et al., 2018; Lovett et al., 2009; Sawyer et al., 2018).

3.2 Functional Characterization of Cardiac Output

To overcome the challenges associated with recording electrical potentials in 3D cultures as well as mitigate the financial hurdle of electrophysiology equipment, video microscopy has been used to measure cardiac frequency (Annabi et al., 2013; Huebsch et al., 2015; Saini et al., 2015). However, this method does not account for the DoC between CM contractions, an important indicator of myocardium maturity. To determine isolated vs. conducted contraction in our 3D μTissues, we developed an automated MATLAB algorithm to measure both CM BPM and DoC. Individual cells were identified within 3D μTissues (**Figure 2A)** and classified as beating or a non-beating cardiac cells based upon inclusion criteria (i.e., signal-to-noise ratio, peak-to-peak frequency; **Figure 2B**). The summation was used to calculate the global BPM for each experimental condition.

The DoC was quantified by assigning each beating CM with a unique cell ID# and plotting the timestamp of each contraction (**Figure 2C**). To quantify DoC, these plots were analyzed with a SPIKE algorithm developed for assessing synchrony in neuron populations (Kreuz et al., 2015). As shown in **Figure 2D**, quantified cell beating using our developed algorithm has a one-to-one correlation with recordings processed using a MEA, demonstrating the robustness of our image analysis tool and that we are detecting CM depolarization (**Supplemental Video 1**). As further validation, μTissues were treated with isoproterenol, a beta-adrenergic agonist to demonstrate the utility of this algorithm to detect a changes in physiological responses (Maoz et al., 2017). A temporal increase in beating frequency (~50%) and decrease in DoC (~10%) was detectable with this video quantification tool (**Figure 2E**).

3.3 Impact of Patterning and Photoinitiator on 3D μTissues

Spontaneous beating was recorded over a period of 9 days for cardiac μTissue constructs formed across all hydrogel samples. Similar to previous findings (Saini et al., 2015), no beating was observed when only enriched populations of CMs were encapsulated within the 3D μTissues (data not shown). μTissues crosslinked with visible light (LAP), on average, exhibited on average a 25% increase in rates of beating for all measured time points compared to Irgacure® controls (**Figure 3A-C**). There were no differences in the DoC were apparent when comparing crosslinking systems irrespective of patterning (**Figure 3B-C**). However, regardless of the crosslinking system implored, the inclusion of aCCs within patterned hydrogels led to spontaneous beating on day 3 post encapsulation vs. day 4 post encapsulation for unpatterned samples (**Figures 3A and 3D**). Lastly, despite the relatively low CM density, patterned 3D μTissues exhibited a statistically

significant ($p < 0.0001$) increase in DoC compared to unpatterned hydrogels throughout the entire study (**Figure 3E-F**).

3.4 SC incorporation in the 3D μTissues

To validate the use of cardiac μTissues for further understanding the role of non-myocyte support cells in the heart, CM functional outputs and morphological differences were assessed with the inclusion of exogenous SCs. Enriched CM and aCC populations were characterized via immunocytochemistry to quantify the endogenous cell composition as a baseline of isolation heterogeneity. As expected, an increased ratio of CMs, identified by sarcomeric α-actinin, were present in the enriched CM suspension (**Figure 4A-C**). The remaining non-adherent (enriched CM suspension) and adherent (aCCs) cells were identified by staining for fibroblasts ($CD90^+$), smooth muscle cells (α-smooth muscle $actin^+$), and SCs ($S100^+$). While, immunostaining demonstrated that both the enriched CM and aCC cultures contained heterogeneous cell populations, this analysis only provides a glimpse of all the cells found in the heart (Gherghiceanu and Popescu, 2012; Nandi and Mishra, 2015; Pinto et al., 2016; Popescu et al., 2015; Zhou and Pu, 2016). However, by the reincorporation of all cell collected from the cardiac dissociation, the cardiac μTissues better recapitulate the cellular composition of an intact myocardium. The proportion of viable $S100^+$ cells isolated from the heart was 19.61 ± 4.08%, which is approximately double of the SC composition previously reported for the human atria (Popescu et al., 2015). This higher than expected value, in part, may be due to false positives, specifically S100 expression in macrophages (Hulsmans et al., 2017).

Injected SCs have demonstrated therapeutic effects on cardiac function following infarction in rodent models (Wang et al., 2012; Zhang et al., 2010). Here, SCs from the sciatic nerve were used to ensure a high concentration and avoid a potential loss of phenotype that has previously been reported for cardiac support cells during expansion (Zuppinger, 2016). Inclusion of SCs led to a significant 2-fold increase ($p < 0.0001$) in the BPM of CMs as compared to controls at all measured time points (**Figure 5A, Figure S4, Supplemental Video 2-3**). Additionally, the inclusion of SCs decreased the DoC from 85.10 ± 0.98% to 76.76 ± 0.99% (**Figure 5B**). These trends were also observed for cardiac cells with/without SCs when cultured on a 2D scaffold (**Figure S5).** There were no observable morphological differences of CMs within the μTissues after the incorporation of SCs (**Figure 5C-D**), yet in 2D cultures, CMs co-cultured with SCs possessed an aspect ratio of 4.1 ± 1.8 compared to 1.6 ± 0.5 for controls without SCs (**Figure 5E-G)**.

3.5 Electrical Pacing of 3D μTissues

Electrical stimulation (ES) to pace the 3D μTissues provided better understand how SCs may influence contraction of the myocardium. ES was applied on day 5 post encapsulation via carbon rod electrodes as previously reported (Tandon et al., 2009). BPM were measured for different frequencies and voltages of applied ES. Prior to ES, encapsulated cardiac cells had an average BPM of 45.27 ± 2.16. Ramping from 1V to 3V to 5V led to an increased response that trended toward the applied frequency for 2 (117.19 ± 8.85) and 3 Hz (153.11 ± 6.95) at 5V (**Figure 6A**). The cardiac μTissues were unable to be paced at 0.5 or 1 Hz for any of the tested voltages. As the rate of spontaneous beating was close to the 1 Hz pacing, the effects of electrical stimulation in this range were indeterminable. The incorporation of SCs into these constructs (average BPM of

60.50 ± 9.51) completely prevented electrical pacing at any of the tested frequencies and voltages (**Figure 6B**). Immunocytochemistry of the co-culture suggests that SCs ability to insulate CMs may in part be due to the formation of connexin junctions between SCs and CMs (**Figure 6C**). Lastly, with the addition of a connexin blocker, heptanol, a small percentage of CMs exhibited increased beat rates when electrically stimulated (**Figure 6D**), which were visually identified following slight increases in averaged beat rate with heptanol treatment (data not shown).

3.6 Modeling of CM-SC Coupling

As evidence by visual analysis of 3D μTissues contractility, SCs influenced the electrophysiological properties of CMs *in vitro*. To further explore this interaction, we modeled CM-SC coupling *in silico* (**Figure 6E**). We first developed a simple SC model by fitting published SC voltage clamp data for a type I potassium channel (Baker and Ritchie, 1996), a L-type calcium channel (Amédée et al., 1991), and a sodium channel (Howe and Ritchie, 1990). Equations for maximum current, channel conductance, activation and inactivate coefficients, and time constants vs. membrane potential were used to simulate voltage clamp experiments for each SC channel (**Figure S6-8**). Coupling the simulated SC to a CM model *in silico* (Sachse et al., 2008) suggested that SCs increase the CM resting potential and accelerates repolarization (**Figure 6F-H**). *In vivo*, a decreased action potential duration for 90% repolarization (APD90) increases the frequency at which a CM can be depolarized (Hulsmans et al., 2017), thereby increasing the maximum beating frequency. However, contrary to our results from electrical pacing, a higher resting potential did not reduce the stimulation threshold necessary to facilitate depolarization.

Discussion

Our developed biomimetic *in vitro* 3D μTissues hold potential to measure functional outputs as cardiac cellular composition is manipulated. This system approaches the resolution of cell printing without subjecting sensitive primary CMs to the temperatures and shear stresses often associated with bioprinting conditions (Blaeser et al., 2016). GelMA allows tunability to mimic native mechanics, possesses protein composition to native myocardium ECM as well as a high availability of cell binding domains, and can be processed into 3D geometries (Yue et al., 2015). But, traditional GelMA crosslinking requires high intensity UV and cytotoxic photoinitiators (Yue et al., 2015) motivating the development of visible light crosslinking systems (Annabi et al., 2017; Fairbanks et al., 2009; Noshadi et al., 2017a; Yue et al., 2015).

EosinY/Triethanolamine is a type II photoinitiator that supports cell viability for encapsulated 3T3 fibroblasts (Noshadi et al., 2017a), but poor viability for primary CMs (Noshadi et al., 2017b) in crosslinked GelMA hydrogels. Type II photoinitiators also require longer photocrosslinking exposure times to achieve the same mechanical properties as type I photoinitiators (Fairbanks et al., 2009), increasing free radicals that can impact viability (Maxwell and Lip, 1997). However, in addition to the photocytotoxicity, Irgacure®, the most common type I photoinitiator used for crosslinking GelMA, is by itself cytotoxic (Fairbanks et al., 2009). Therefore, we investigated the use of LAP, a commercially available visible light type I photoinitiation, for the development of our cardiac μTissues. GelMA hydrogels formed with either photoinitiator (LAP and Irgacure®) exhibited similar mechanical properties (**Figure S2B**), within the ranges (~1 – 80 kPa) previously reported (Yue et al., 2015). Primary cardiac cells encapsulated in GelMA hydrogels using LAP

and visible light possessed higher cell viability than those formed by using UV light and/or Irgacure® (**Figure 1C**), as reported previously in other cells (Fairbanks et al., 2009).

Correlating in-the-dish measures of contractility to cardiac output and health is paramount for the long-term utility of *in vitro* cardiac models. BPM, DoC, and conduction velocity have been exclusively measured electrically (Natarajan et al., 2011). However, methods for intra and extracellular recordings require expensive equipment, specialized expertise, and use of these techniques with 3D μTissues provides additional technical challenges, such as reduced signal-to-noise ratios, low-throughput, and cell damage during the penetration of glass electrodes into the 3D μTissues (Tonomura et al., 2010). Attempts to overcome these limitations have yielded some success by measuring contractions via video microscopy (Annabi et al., 2013; Huebsch et al., 2015; Saini et al., 2015) or cantilevers (Boudou et al., 2012; Morimoto et al., 2013; Uzel et al., 2016). In each of these cases, beating frequency is measured by counting the global changes in intensity, size, and/or force measurements over a set duration. These techniques fail to directly measure variability across individual beating cells, thus quantification of coordination and conduction velocity remain out of reach. Here, we developed a custom processing technique that allows for cardiac function to be assessed on a per cell basis that renders comparable results to traditional electrophysiology (**Figure 2**). Further, due to our non-destructive imaging of cardiac beating, this approach may be used in combination with the previously mentioned techniques to correlate macroscopic function to intracellular interactions in both 2D and 3D culture systems. Our algorithm is capable of calculating conduction velocity, but accurate measures rely on frame rates faster than 200 frames per second to determine differences between cells, speeds which lies beyond the capabilities of most camera systems.

Towards investigating the effects of cardiac architecture, the role of patterning was assessed as an approach to improve function, specifically DoC. Maintaining coordinated beating in the heart is required *in vivo* to pump blood throughout the body, thus DoC is a critical metric to quantify for the establishment of cardiac μTissues. Previous studies have suggested local CM alignment is required to support synchronous beating and can be improved with micropatterned features having widths less than 100 μm (Saini et al., 2015; Salick et al., 2014). Here, to study the sole impact of mesoscale architecture on DoC, μTissues were developed with widths of 500 μm. As expected, there was no improved local, cellular alignment within patterned cardiac μTissues, but alignment of the cell-laden substrate resulted in an increase in DoC. Therefore, despite not exhibiting an alignment of CM along a single axis, patterned cardiac μTissues possess a higher degree of functionality towards recapitulating the native myocardium.

To understand how SCs might affect cardiomyocyte phenotype, we incorporated both primary SC and CM into μTissues. SCs are non-neural support cells that play an essential role in neuron signaling and regeneration (Armati and Mathey, 2013). SCs have been evaluated at the bench as a cell therapy for cardiac failure (Wang et al., 2012; Zhang et al., 2010) and make up a substantial composition of the heart (Gherghiceanu and Popescu, 2012; Popescu et al., 2015). Often cells isolated from the heart are characterized as either CMs or cardiac FBs (Annabi et al., 2016; Annabi et al., 2013; Noshadi et al., 2017a; Noshadi et al., 2017b; Saini et al., 2015; Shin et al., 2016), but in fact these populations are heterogeneous and contain fewer than 20% FBs. For this reason, we established a new nomenclature for this cell isolation protocol in which suspension cells are

referred to as enriched CMs and the adherent cells are referred to as adherent cardiac cells (aCCs). Further, the presence of these aCCs is critical for developing functional engineered cardiac tissues from stem cells (Iseoka et al., 2018).

CMs co-cultured with SCs in standard 2D conditions exhibited an increased aspect ratio (between 5 and 9.5; **Figure 5A-C**), typical of a more mature CM phenotype (Denning et al., 2016). Qualitatively, CMs cultured with SCs present with more clearly defined z-disks, evidenced by localization of α-actinin, elongation of nuclei, and a possible an increase in bi-nucleation (**Figure S9**): indicators of CM differentiation and maturation (Scuderi and Butcher, 2017; Zebrowski et al., 2017). In response to peripheral nerve damage, non-myelinating SCs provide topographical cues that influence the rate and direction of neurite outgrowth (Hoffman-Kim et al., 2010), with monolayers of SCs exhibiting beneficial local alignment that impacts sensory neuron growth *in vitro* (Seggio et al., 2010). CMs may exhibit a higher aspect ratio via similar structural cues. Peculiar to this observation of increased CM differentiation, the presence of exogenous SCs increased the average BPM as well as a decrease the DoC in cardiac μTissues (**Figure 5F-G**), similar to higher BPM observed during development (Lindsey et al., 2014). However, immunofluorescent images of the CMs within the cardiac μTissues containing exogenous SCs did exhibit the higher aspect ratios observed in 2D cultures (**Figure 5C-D**). Within a 3D scaffold, the mechanical microenvironment, specifically the increase in cell-ECM adhesions, may limit the influence of SC structure on CM morphology. Additionally, SC proliferation rate may be slowed (Edmondson et al., 2014), limiting the density of SCs to promote local CM alignment. In addition to providing guidance cues, SCs also overexpress matrix metalloproteinases (MMPs) following a nerve injury (Liu et al., 2010; Parrinello et al., 2010). Therefore, due to an abundance of MMP-

sensitive degradation sequences in gelatin (Vandooren et al., 2013), the inclusion of SCs may alter the mechanical properties of our μTissues over time, which may also influence cardiac phenotype and contraction (Bhana et al., 2010). This reduction in mechanical stability was confirmed observationally by the increase degradation and delamination of the μTissues from the glass slides after 9 days (**Figure S10**). Nevertheless, similar contractile trends were observed when cells were cultured on 2D scaffolds compared to those cultured in 3D, ruling out confounding effects of material degradation (**Figure S5**).

Developing mammalian hearts beat at higher rates due a higher ratio of connective tissue to muscle or aCCs to CMs, immature T-tubule and sarcoplasmic reticulum, and a higher concentration of plasma calcium (Louch et al., 2015). CM contraction is predominantly regulated by intracellular Ca^{2+} concentration cycling and a resultant membrane depolarization, that in mature CM constructs originates with an atrial pacemaker and progresses to surrounding cells with a high DoC. Non-myelinating SCs exhibit excitable properties including regulating Ca^{2+} in neuromuscular junctions (Reist and Smith, 1992) and K^{+} in the axonal microenvironment (Robert and Jirounek, 1994). While SC presence in the heart has recently been highlighted, their role on plasma and cytosol ion dynamics in the myocardium remains unknown.

When external electrical stimulation was applied to 3D μTissues, SCs prevented the CMs within the μTissues from being externally paced. Similarly, Zhang *et al.* reported that the injection of exogenous SCs into the heart reduced the occurrence of electrically induced arrhythmias (Zhang et al., 2010). We hypothesize that SCs, which are known to express connexin proteins (Nicholson

and Bruzzone, 1997), form connexin junctions with some CMs (**Figure 6C**), therefore increasing the resting potential and allowing for a more rapid depolarization and subsequent contraction and expansion. This mechanism of CMs forming connexin junctions with other cells is demonstrated by a recent report in which cardiac macrophages are shown to increase the CM resting potential (Hulsmans et al., 2017). While SCs maintain a higher resting membrane potential compared to CMs (-40 mV for SCs (Baker and Ritchie, 1996; Howe and Ritchie, 1990) vs. -80 mV for CMs (Sachse et al., 2008)), SCs also contain ion channels for Ca^{2+} and Na^{+} in addition to similar K^{+} channels to those in cardiac macrophages. Therefore, it is expected that in addition to an increased resting potential, the CM electrophysiological properties will be significantly altered by SC coupling.

Executing a CM-SC *in silico* model revealed that the initial depolarization of the SC membrane with CM depolarization led to an overcorrection to repolarize the SC membrane, which helped to quicken the CM repolarization. However, with increased coupling, the rate at which a CM is repolarized returned to its initial APD90, thereby suggesting an enhanced ability for CMs coupled with SCs to better regulate their membrane potential, while initial resting potential continues to increase. Lastly, when treated with a general connexin blocker, heptanol (Brokamp et al., 2012), a small percentage of CMs responded to external, pulsatile electrical stimulus while non-blocked SC-CM cultures did not (**Figure 6D**). These cells were visually identified and analyzed. While the proximity of these identified CMs to SCs was not known during live video recordings, this finding may support SCs ability to electrically couple to CMs via gap junctions, similar to that observed with fibroblasts (Sachse et al., 2008) and macrophages (Hulsmans et al., 2017). However, the

mechanism which leads to increased beating and diminished coordination requires further investigation.

In conclusion, our 3D μTissues provide a cardiac cell-supporting microenvironment by better mimicking the function and cellular composition of the heart, which is critical for the development of cell and tissue engineering therapeutic strategies (Cimetta et al., 2013). Furthermore, this platform can be exploited to investigate the multicellular composition of the heart via the inclusion of exogenous cell populations. Specially, utilizing this approach in combination with computational modeling, we demonstrated that SCs may play a critical role in CM maturation and as electrical insulators in the heart. This system may provide a means to model human physiology and pathology through the incorporation of stem cell derived cardiac cell populations. All together, these approaches in conjunction with computational models, quantitative cardiac outputs, and low capital expensive will hopefully lead to a more widespread use of microphysiological systems, which can be utilized to increase translation of novel therapies to the clinic. All algorithms for both analysis and modeling can downloaded from http://www.northeastern.edu/lnnr.

Acknowledgements

This work was supported by American Heart Association (AHA) Grant #19PRE34430181 (J.R. Soucy). R.A.K. and N.A. acknowledge Northeastern University and the startup fund provided by the Department of Chemical Engineering, College of Engineering at Northeastern University. R.A.K. further acknowledges the support from the National Institutes of Health (NIH, R21EB025395-01) and N.A. acknowledges the support from the AHA (16SDG31280010) and the NIH (R01-EB023052/O1A1).

Author information

Affiliations

Department of Chemical Engineering, Northeastern University, Boston, MA 02115, USA

Jonathan R. Soucy, Jody Askaryan, David Diaz, Abigail N. Koppes, Nasim Annabi, Ryan A. Koppes

Department of Biology, Northeastern University, Boston, MA 02115, USA

Abigail N. Koppes

Department of Chemical and Biomolecular Engineering, University of California- Los Angeles, Los Angeles, CA 90095; Center for Minimally Invasive Therapeutics (C-MIT), University of California-Los Angeles, Los Angeles, CA 90095; Harvard-MIT Division of Health Sciences and Technology, Massachusetts Institute of Technology, Cambridge, MA 02139, USA

Nasim Annabi

Contributions

J.R.S., N.A., and R.A.K. conceived the project. J.R.S. synthesized and characterized materials, isolated neonatal rat cardiac cells, stained and imaged all samples, developed the MATLAB algorithm, and wrote the electrophysiology stimulation. J.R.S. completed the *in vitro* cell studies with assistance from J.A. D.D. isolated and purified and SCs from neonatal rats under the advisement of A.N.K. A.N.K provided intellectual input and advice. J.R.S. and R.A.K. analyzed the results, prepared the figures, and wrote the manuscript. All authors edited and provided feedback on the manuscript. R.A.K. and N.A. supervised the work.

Competing interests

The authors declare no competing interests.

Corresponding author

Correspond to Ryan A. Koppes

r.koppes@northeastern.edu

Nasim Annabi

n.annabi@northeastern.edu

References

Amédée, T., Ellie, E., Dupouy, B., and Vincent, J.D. (1991). Voltage-dependent calcium and potassium channels in Schwann cells cultured from dorsal root ganglia of the mouse. The Journal of Physiology *441*, 35-56.

Annabi, N., Rana, D., Shirzaei Sani, E., Portillo-Lara, R., Gifford, J.L., Fares, M.M., Mithieux, S.M., and Weiss, A.S. (2017). Engineering a sprayable and elastic hydrogel adhesive with antimicrobial properties for wound healing. Biomaterials *139*, 229-243.

Annabi, N., Shin, S.R., Tamayol, A., Miscuglio, M., Bakooshli, M.A., Assmann, A., Mostafalu, P., Sun, J.Y., Mithieux, S., Cheung, L.*, et al.* (2016). Highly Elastic and Conductive Human-Based Protein Hybrid Hydrogels. Adv Mater *28*, 40-49.

Annabi, N., Tsang, K., Mithieux, S.M., Nikkhah, M., Ameri, A., Khademhosseini, A., and Weiss, A.S. (2013). Highly Elastic Micropatterned Hydrogel for Engineering Functional Cardiac Tissue. Adv Funct Mater *23*, 4950-4959.

Armati, P.J., and Mathey, E.K. (2013). An update on Schwann cell biology--immunomodulation, neural regulation and other surprises. J Neurol Sci *333*, 68-72.

Armour, A.J. (1991). Intrinsic Cardiac Neurons. Journal of Cardiovascular Electrophysiology *2*, 331-341.

Baker, M.D., and Ritchie, J.M. (1996). Characteristics of type I and type II K+ channels in rabbit cultured Schwann cells. The Journal of physiology *490 (Pt 1)*, 79-95.

Barik, A., Li, L., Sathyamurthy, A., Xiong, C.W., and Mei, L. (2016). Schwann Cells in Neuromuscular Junction Formation and Maintenance. J Neurosci *36*, 9770-9781.

Bhana, B., Iyer, R.K., Chen, W.L., Zhao, R., Sider, K.L., Likhitpanichkul, M., Simmons, C.A., and Radisic, M. (2010). Influence of substrate stiffness on the phenotype of heart cells. Biotechnol Bioeng *105*, 1148-1160.

Björnson, E., Borén, J., and Mardinoglu, A. (2016). Personalized Cardiovascular Disease Prediction and Treatment—A Review of Existing Strategies and Novel Systems Medicine Tools. Frontiers in Physiology *7*, 2.

Blaeser, A., Campos, D., Puster, U., Richtering, W., Stevens, M.M., and Fischer, H. (2016). Controlling Shear Stress in 3D Bioprinting is a Key Factor to Balance Printing Resolution and Stem Cell Integrity. Advanced Healthcare Materials *5*, 326-333.

Boudou, T., Legant, W.R., Mu, A., Borochin, M.A., Thavandiran, N., Radisic, M., Zandstra, P.W., Epstein, J.A., Margulies, K.B., and Chen, C.S. (2012). A Microfabricated Platform to Measure and Manipulate the Mechanics of Engineered Cardiac Microtissues. Tissue Eng Part A *18*, 910-919.

Brokamp, C., Todd, J., Montemagno, C., and Wendell, D. (2012). Electrophysiology of Single and Aggregate Cx43 Hemichannels. PLoS One *7*.

Cimetta, E., Godier-Furnémont, A., and Vunjak-Novakovic, G. (2013). Bioengineering heart tissue for in vitro testing. Curr Opin Biotechnol *24*, 926-932.

DeForest, C.A., Polizzotti, B.D., and Anseth, K.S. (2009). Sequential click reactions for synthesizing and patterning three-dimensional cell microenvironments. Nat Mater *8*.

Denning, C., Borgdorff, V., Crutchley, J., Firth, K.S., George, V., Kalra, S., Kondrashov, A., Hoang, M.D., Mosqueira, D., Patel, A.*, et al.* (2016). Cardiomyocytes from human pluripotent stem cells: From laboratory curiosity to industrial biomedical platform. BBA *1863*, 1728-1748.

Edmondson, R., Broglie, J.J., Adcock, A.F., and Yang, L. (2014). Three-dimensional cell culture systems and their applications in drug discovery and cell-based biosensors. Assay Drug Dev Technol *12*, 207-218.

Fairbanks, B.D., Schwartz, M.P., Bowman, C.N., and Anseth, K.S. (2009). Photoinitiated polymerization of PEG-diacrylate with lithium phenyl-2,4,6-trimethylbenzoylphosphinate: polymerization rate and cytocompatibility. Biomaterials *30*, 6702-6707.

Figueiredo, L., Pace, R., D'Arros, C., Rethore, G., Guicheux, J., Le Visage, C., and Weiss, P. (2018). Assessing glucose and oxygen diffusion in hydrogels for the rational design of 3D stem cell scaffolds in regenerative medicine. J Tissue Eng Regen Med *12*, 1238-1246.

Gherghiceanu, M., and Popescu, L.M. (2012). Cardiac telocytes — their junctions and functional implications. Cell and Tissue Research *348*, 265-279.

Gonzalez-Diaz, E.C., and Varghese, S. (2016). Hydrogels as Extracellular Matrix Analogs. Gels *2*.

Hashimoto, H., Olson, E.N., and Bassel-Duby, R. (2018). Therapeutic approaches for cardiac regeneration and repair. Nat Rev Cardiol *15*, 585-600.

Hatzistergos, K.E., and Vedenko, A. (2017). Cardiac Cell Therapy 3.0: The Beginning of the End or the End of the Beginning? Circ Res *121*, 95-97.

Hoffman-Kim, D., Mitchel, J.A., and Bellamkonda, R.V. (2010). Topography, cell response, and nerve regeneration. Annu Rev Biomed Eng *12*, 203-231.

Howe, J.R., and Ritchie, J.M. (1990). Sodium currents in Schwann cells from myelinated and non-myelinated nerves of neonatal and adult rabbits. The Journal of physiology *425*, 169-210.

Huebsch, N., Loskill, P., Mandegar, M.A., Marks, N.C., Sheehan, A.S., Ma, Z., Mathur, A., Nguyen, T.N., Yoo, J.C., Judge, L.M*., et al.* (2015). Automated Video-Based Analysis of Contractility and Calcium Flux in Human-Induced Pluripotent Stem-Derived Cardiomyocytes Cultured over Different Spatial Scales. Tissue Engineering Part C: Methods *21*, 467-479.

Hulsmans, M., Clauss, S., Xiao, L., Aguirre, A.D., King, K.R., Hanley, A., Hucker, W.J., Wülfers, E.M., Seemann, G., Courties, G*., et al.* (2017). Macrophages Facilitate Electrical Conduction in the Heart. Cell *169*, 510.

Iseoka, H., Miyagawa, S., Fukushima, S., Saito, A., Masuda, S., Yajima, S., Ito, E., Sougawa, N., Takeda, M., Harada, A*., et al.* (2018). Pivotal Role of Non-cardiomyocytes in Electromechanical and Therapeutic Potential of Induced Pluripotent Stem Cell-Derived Engineered Cardiac Tissue. Tissue Eng Part A *24*, 287-300.

Kacarevic, Z.P., Rider, P.M., Alkildani, S., Retnasingh, S., Smeets, R., Jung, O., Ivanisevic, Z., and Barbeck, M. (2018). An Introduction to 3D Bioprinting: Possibilities, Challenges and Future Aspects. Materials (Basel) *11*.

Koppes, A.N., Nordberg, A.L., Paolillo, G.M., Goodsell, N.M., Darwish, H.A., Zhang, L., and Thompson, D.M. (2014). Electrical stimulation of schwann cells promotes sustained increases in neurite outgrowth. Tissue Eng Part A *20*, 494-506.

Kreuz, T., Mulansky, M., and Bozanic, N. (2015). SPIKY: a graphical user interface for monitoring spike train synchrony. J Neurophysiol *113*, 3432-3445.

Lee, K.F., Simon, H., Chen, H., Bates, B., Hung, M.C., and Hauser, C. (1995). Requirement for neuregulin receptor erbB2 in neural and cardiac development. Nature *378*, 394-398.

Li, X., Valadez, A.V., Zuo, P., and Nie, Z. (2012). Microfluidic 3D cell culture: potential application for tissue-based bioassays. Bioanalysis *4*, 1509-1525.

Lindsey, S.E., Butcher, J.T., and Yalcin, H.C. (2014). Mechanical regulation of cardiac development. Front Physiol *5*, 318.

Liu, H., Kim, Y., Chattopadhyay, S., Shubayev, I., Dolkas, J., and Shubayev, V.I. (2010). Matrix metalloproteinase inhibition enhances the rate of nerve regeneration in vivo by promoting dedifferentiation and mitosis of supporting schwann cells. J Neuropathol Exp Neurol *69*, 386-395.

Louch, W.E., Koivumäki, J.T., and Tavi, P. (2015). Calcium signalling in developing cardiomyocytes: implications for model systems and disease. The Journal of Physiology *593*, 1047-1063.

Lovett, M., Lee, K., Edwards, A., and Kaplan, D.L. (2009). Vascularization strategies for tissue engineering. Tissue Eng Part B Rev *15*, 353-370.

Malliaras, K., and Marbán, E. (2011). Cardiac cell therapy: where we've been, where we are, and where we should be headed. British Medical Bulletin *98*, 161-185.

Mandrycky, C., Wang, Z., Kim, K., and Kim, D.-H. (2016). 3D bioprinting for engineering complex tissues. Biotechnol Adv *34*, 422-434.

Maoz, B.M., Herland, A., Henry, O.Y.F., Leineweber, W.D., Yadid, M., Doyle, J., Mannix, R., Kujala, V.J., FitzGerald, E.A., Parker, K.*, et al.* (2017). Organs-on-Chips with combined multi-electrode array and transepithelial electrical resistance measurement capabilities. Lab Chip *17*, 2294-2302.

Maxwell, S.R., and Lip, G.Y. (1997). Free radicals and antioxidants in cardiovascular disease. British journal of clinical pharmacology *44*, 307-317.

Mayourian, J., Savizky, R.M., Sobie, E.A., and Costa, K.D. (2016). Modeling Electrophysiological Coupling and Fusion between Human Mesenchymal Stem Cells and Cardiomyocytes. PLoS Comput Biol *12*.

Mitcheson, J.S., Hancox, J.C., and Levi, A.J. (1998). Cultured adult cardiac myocytes: Future applications, culture methods, morphological and electrophysiological properties. Cardiovascular Research *39*, 280-300.

Morimoto, Y., Kato-Negishi, M., Onoe, H., and Takeuchi, S. (2013). Three-dimensional neuron-muscle constructs with neuromuscular junctions. Biomaterials *34*, 9413-9419.

Morris, J.K., Lin, W., Hauser, C., Marchuk, Y., Getman, D., and Lee, K.F. (1999). Rescue of the cardiac defect in ErbB2 mutant mice reveals essential roles of ErbB2 in peripheral nervous system development. Neuron *23*, 273-283.

Muller, P., Lemcke, H., and David, R. (2018). Stem Cell Therapy in Heart Diseases - Cell Types, Mechanisms and Improvement Strategies. Cell Physiol Biochem *48*, 2607-2655.

Nandi, S.S., and Mishra, P.K. (2015). Harnessing fetal and adult genetic reprograming for therapy of heart disease. Journal of nature and science *1*.

Naseer, S.M., Manbachi, A., Samandari, M., Walch, P., Gao, Y., Zhang, Y.S., Davoudi, F., Wang, W., Abrinia, K., Cooper, J.M.*, et al.* (2017). Surface acoustic waves induced micropatterning of cells in gelatin methacryloyl (GelMA) hydrogels. Biofabrication *9*, 015020.

Natarajan, A., Stancescu, M., Dhir, V., Armstrong, C., Sommerhage, F., Hickman, J.J., and Molnar, P. (2011). Patterned cardiomyocytes on microelectrode arrays as a functional, high information content drug screening platform. Biomaterials *32*, 4267-4274.

Nichol, J.W., Koshy, S.T., Bae, H., Hwang, C.M., Yamanlar, S., and Khademhosseini, A. (2010). Cell-laden microengineered gelatin methacrylate hydrogels. Biomaterials *31*, 5536-5544.

Nicholson, S.M., and Bruzzone, R. (1997). Gap junctions: Getting the message through. Current Biology *7*.

Noshadi, I., Hong, S., Sullivan, K.E., Sani, E., Portillo-Lara, R., Tamayol, A., Shin, S., Gao, A.E., Stoppel, W.L., Iii, L.D., *et al.* (2017a). In vitro and in vivo analysis of visible light crosslinkable gelatin methacryloyl (GelMA) hydrogels. Biomaterials Science *5*, 2093-2105.

Noshadi, I., Walker, B.W., Portillo-Lara, R., Sani, E., Gomes, N., Aziziyan, M., and Annabi, N. (2017b). Engineering Biodegradable and Biocompatible Bio-ionic Liquid Conjugated Hydrogels with Tunable Conductivity and Mechanical Properties. Scientific Reports *7*, 4345.

Parrinello, S., Napoli, I., Ribeiro, S., Wingfield Digby, P., Fedorova, M., Parkinson, D.B., Doddrell, R.D., Nakayama, M., Adams, R.H., and Lloyd, A.C. (2010). EphB signaling directs peripheral nerve regeneration through Sox2-dependent Schwann cell sorting. Cell *143*, 145-155.

Pawlak, M., Niescierowicz, K., and Winata, C.L. (2018). Decoding the Heart through Next Generation Sequencing Approaches. Genes (Basel) *9*.

Perbellini, F., Watson, S.A., Bardi, I., and Terracciano, C.M. (2018). Heterocellularity and Cellular Cross-Talk in the Cardiovascular System. Front Cardiovasc Med *5*, 143.

Pinto, A.R., Ilinykh, A., Ivey, M.J., Kuwabara, J.T., D'Antoni, M.L., Debuque, R., Chandran, A., Wang, L., Arora, K., Rosenthal, N.A., *et al.* (2016). Revisiting Cardiac Cellular Composition. Circ Res *118*, 400-409.

Popescu, L.M., Curici, A., Wang, E., Zhang, H., Hu, S., and Gherghiceanu, M. (2015). Telocytes and putative stem cells in ageing human heart. Journal of Cellular and Molecular Medicine *19*, 31-45.

Ravi, M., Paramesh, V., Kaviya, S.R., Anuradha, E., and Solomon, F.D. (2015). 3D cell culture systems: advantages and applications. J Cell Physiol *230*, 16-26.

Reist, N.E., and Smith, S.J. (1992). Neurally evoked calcium transients in terminal Schwann cells at the neuromuscular junction. Proc Natl Acad Sci U S A *89*, 7625-7629.

Robert, A., and Jirounek, P. (1994). Uptake of potassium by nonmyelinating Schwann cells induced by axonal activity. J Neurophysiol *72*, 2570-2579.

Sachse, F.B., Moreno, A.P., and Abildskov, J.A. (2008). Electrophysiological Modeling of Fibroblasts and their Interaction with Myocytes. Ann Biomed Eng *36*, 41-56.

Saini, H., Navaei, A., Van Putten, A., and Nikkhah, M. (2015). 3D cardiac microtissues encapsulated with the co-culture of cardiomyocytes and cardiac fibroblasts. Adv Healthc Mater *4*, 1961-1971.

Salick, M.R., Napiwocki, B.N., Sha, J., Knight, G.T., Chindhy, S.A., Kamp, T.J., Ashton, R.S., and Crone, W.C. (2014). Micropattern width dependent sarcomere development in human ESC-derived cardiomyocytes. Biomaterials *35*, 4454-4464.

Sawyer, S.W., Shridhar, S.V., Zhang, K., Albrecht, L.D., Filip, A.B., Horton, J.A., and Soman, P. (2018). Perfusion directed 3D mineral formation within cell-laden hydrogels. Biofabrication *10*, 035013.

Scuderi, G.J., and Butcher, J. (2017). Naturally Engineered Maturation of Cardiomyocytes. Front Cell Dev Biol *5*, 50.

Seggio, A.M., Narayanaswamy, A., Roysam, B., and Thompson, D.M. (2010). Self-aligned Schwann cell monolayers demonstrate an inherent ability to direct neurite outgrowth. J Neural Eng *7*, 46001.

Sheng, J., Shim, W., Lu, J., Lim, S., Ong, B., Lim, T., Liew, R., Chua, Y., and Wong, P. (2014). Electrophysiology of human cardiac atrial and ventricular telocytes. Journal of Cellular and Molecular Medicine *18*, 355-362.

Shin, S., Zihlmann, C., Akbari, M., Assawes, P., Cheung, L., Zhang, K., Manoharan, V., Zhang, Y., Yüksekkaya, M., Wan, K.t., *et al.* (2016). Reduced Graphene Oxide-GelMA Hybrid Hydrogels as Scaffolds for Cardiac Tissue Engineering. Small *12*, 3677-3689.

Skelly, D.A., Squiers, G.T., McLellan, M.A., Bolisetty, M.T., Robson, P., Rosenthal, N.A., and Pinto, A.R. (2018). Single-Cell Transcriptional Profiling Reveals Cellular Diversity and Intercommunication in the Mouse Heart. Cell Rep *22*, 600-610.

Soucy, J.R., Ehsan, S., Roberto, P., David, D., Felipe, D., Weiss, A.S., Koppes, A.N., Koppes, R.A., and Nasim, A. (2018). Photocrosslinkable Gelatin/Tropoelastin Hydrogel Adhesives for Peripheral Nerve Repair. Tissue Eng Part A.

Tandon, N., Cannizzaro, C., Chao, P.-H.G.H., Maidhof, R., Marsano, A., Au, H.T., Radisic, M., and Vunjak-Novakovic, G. (2009). Electrical stimulation systems for cardiac tissue engineering. Nat Protoc *4*, 155-173.

Tang, J.N., Cores, J., Huang, K., Cui, X.L., Luo, L., Zhang, J.Y., Li, T.S., Qian, L., and Cheng, K. (2018). Concise Review: Is Cardiac Cell Therapy Dead? Embarrassing Trial Outcomes and New Directions for the Future. Stem Cells Transl Med *7*, 354-359.

Tibbitt, M.W., and Anseth, K.S. (2009). Hydrogels as extracellular matrix mimics for 3D cell culture. Biotechnol Bioeng *103*, 655-663.

Tonomura, W., Shimizu, K., and Konishi, S. (2010). Electrophysiological recordings using spatially arranged microelectrode probes embedded into 3-D neuronal cultures. Proc of MicroTAS2010.

Uzel, S.G., Platt, R.J., Subramanian, V., Pearl, T.M., Rowlands, C.J., Chan, V., Boyer, L.A., So, P.T., and Kamm, R.D. (2016). Microfluidic device for the formation of optically excitable, three-dimensional, compartmentalized motor units. Sci Adv *2*, e1501429.

Vandooren, J., Van den Steen, P.E., and Opdenakker, G. (2013). Biochemistry and molecular biology of gelatinase B or matrix metalloproteinase-9 (MMP-9): the next decade. Crit Rev Biochem Mol Biol *48*, 222-272.

Wang, Y., Zhang, G., Hou, Y., Chen, J., Wang, J., Zou, C., Li, D., Li, H., Zhang, Q., Wang, A.*, et al.* (2012). Transplantation of microencapsulated Schwann cells and mesenchymal stem cells augment angiogenesis and improve heart function. Mol Cell Biochem *366*, 139-147.

Wanjare, M., and Huang, N.F. (2017). Regulation of the microenvironment for cardiac tissue engineering. Regen Med *12*, 187-201.

Xin, M., Olson, E.N., and Bassel-Duby, R. (2013). Mending broken hearts: cardiac development as a basis for adult heart regeneration and repair. Nat Rev Mol Cell Biol *14*.

Yue, K., Trujillo-de Santiago, G., Alvarez, M.M., Tamayol, A., Annabi, N., and Khademhosseini, A. (2015). Synthesis, properties, and biomedical applications of gelatin methacryloyl (GelMA) hydrogels. Biomaterials *73*, 254-271.

Zamani, M., Karaca, E., and Huang, N.F. (2018). Multicellular Interactions in 3D Engineered Myocardial Tissue. Front Cardiovasc Med *5*, 147.

Zebrowski, D.C., Jensen, C.H., Becker, R., Ferrazzi, F., Baun, C., Hvidsten, S., Sheikh, S.P., Polizzotti, B.D., Andersen, D.C., and Engel, F.B. (2017). Cardiac injury of the newborn mammalian heart accelerates cardiomyocyte terminal differentiation. Sci Rep *7*, 8362.

Zhang, H., Yuan, X., Jin, P.F., Hou, J.F., Wang, W., Wei, Y.J., and Hu, S. (2010). Alteration of parasympathetic/sympathetic ratio in the infarcted myocardium after Schwann cell transplantation modified electrophysiological function of heart: a novel antiarrhythmic therapy. Circulation *122*, S193-200.

Zhou, P., and Pu, W.T. (2016). Recounting Cardiac Cellular Composition. Circ Res *118*, 368-370.

Zuppinger, C. (2016). 3D culture for cardiac cells. Biochimica et Biophysica Acta (BBA) - Molecular Cell Research *1863*, 1873-1881.

Zuppinger, C. (2019). 3D Cardiac Cell Culture: A Critical Review of Current Technologies and Applications. Front Cardiovasc Med *6*, 87.

Figures

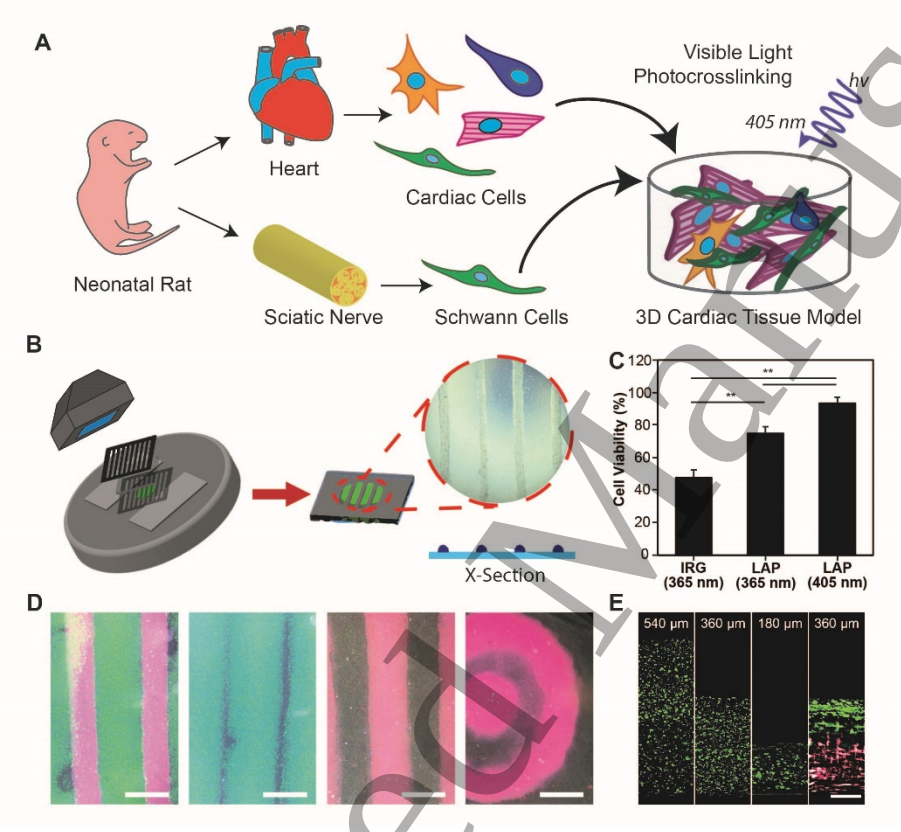

Figure 1. Cardiac µTissue development. (A) Schematic representation of the in vitro co-culture system to investigate the heterogeneity of the myocardium. **(B)** Schematic of photopatterning hydrogels using visible light. **(C)** Quantification of live/dead images show >90% cardiac cell viability in GelMA crosslinked using LAP with visible light (** $p < 0.05$). IRG: Irgacure® 2959. LAP: phenyl-2,4,6-trimethylbenzoylphosphinate. **(D)** Representative images demonstrating an ability to photopattern a range of geometries (scale = 1000 µm) and **(E)** heights, including layers of different compositions, as shown by cross-sections of the 3D µTissues (scale = 100 µm).

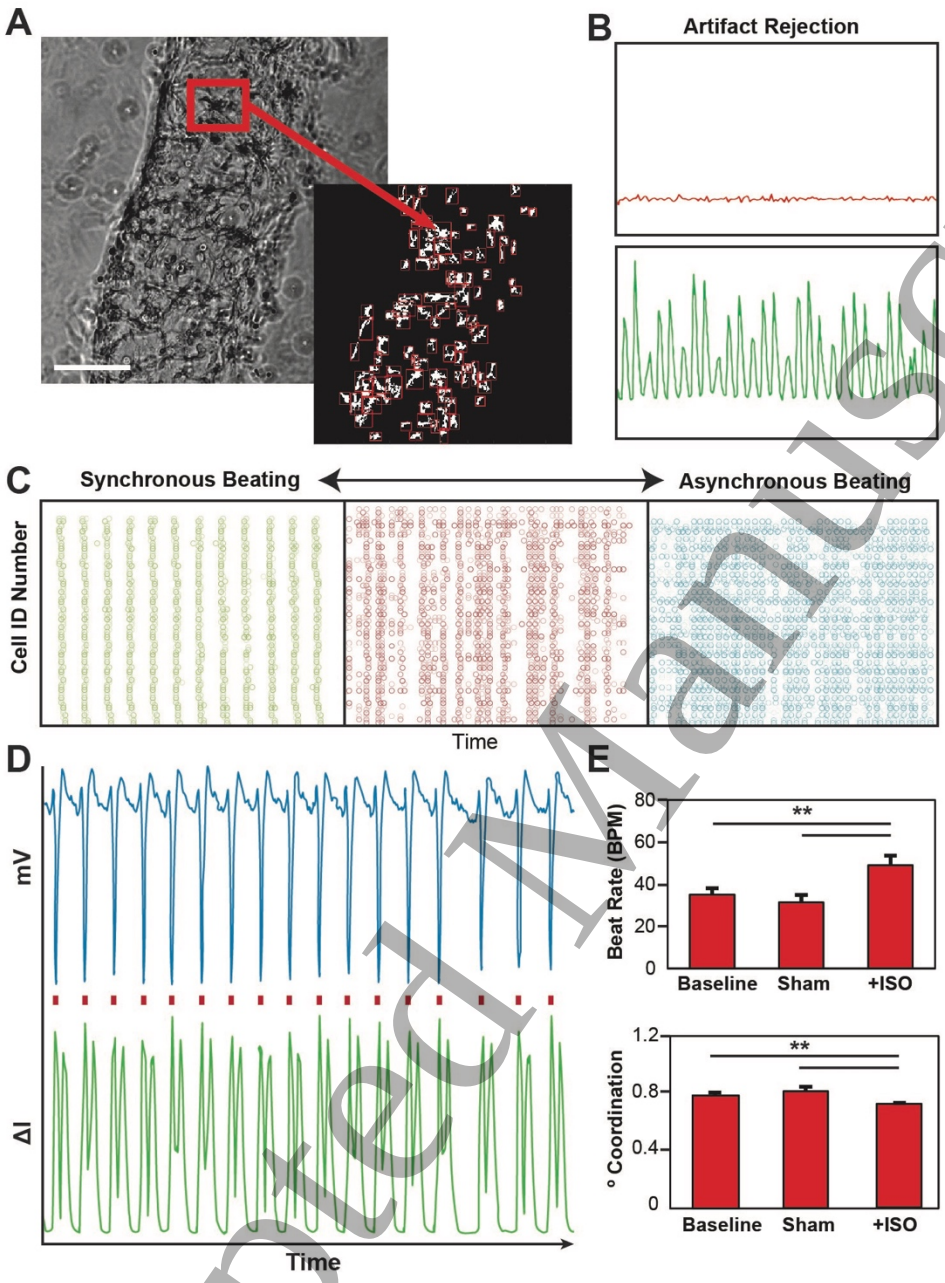

Figure 2. Cardiac beating quantification via video microcopy. (A) Representative bright field image with automated identification of encapsulated cells (scale = 200 μm). **(B)** Representative plots showing the change pixel intensity over time for both a beating and non-beating cell. **(C)** Representative spike train analog used to quantify the degree of coordinated contractions (green =

high level of synchrony, red = some semblance synchrony, blue = no apparent synchrony). **(D)** Validation of beating quantification shows a one-for-one correlation with electrophysiology recordings. **(E)** Isoproterenol treatment of encapsulated cardiac cells shows an expected increase in beat rate and a decrease in synchrony measured via video microcopy (** $p < 0.05$).

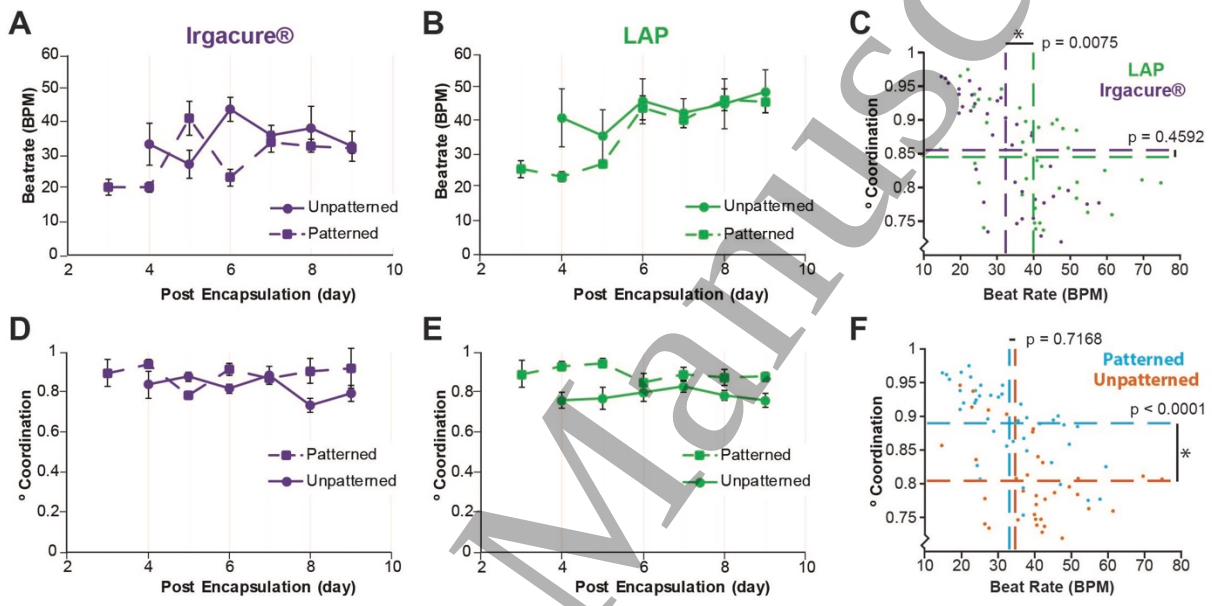

Figure 3. Model development informed by cardiac output quantification. (A) Quantification of beat rate for cardiac cells encapsulated in unpatterned and patterned hydrogels over time using a UV (Irgacure® and 365 nm) or **(B)** a visible (LAP and 405 nm) or crosslinking system. **(C)** Multi-way ANOVA showing statistical differences between the visible and UV crosslinking systems for beat rate, but not coordination. **(D)** Quantification of DoC for cardiac cells encapsulated in patterned or unpatterned hydrogels formed using a UV (Irgacure® and 365nm) or **(E)** visible light (LAP and 405nm) crosslinking system. **(F)** Multi-way ANOVA showing statistical differences between patterned and unpatterned samples for beating coordination, but not beat rate.

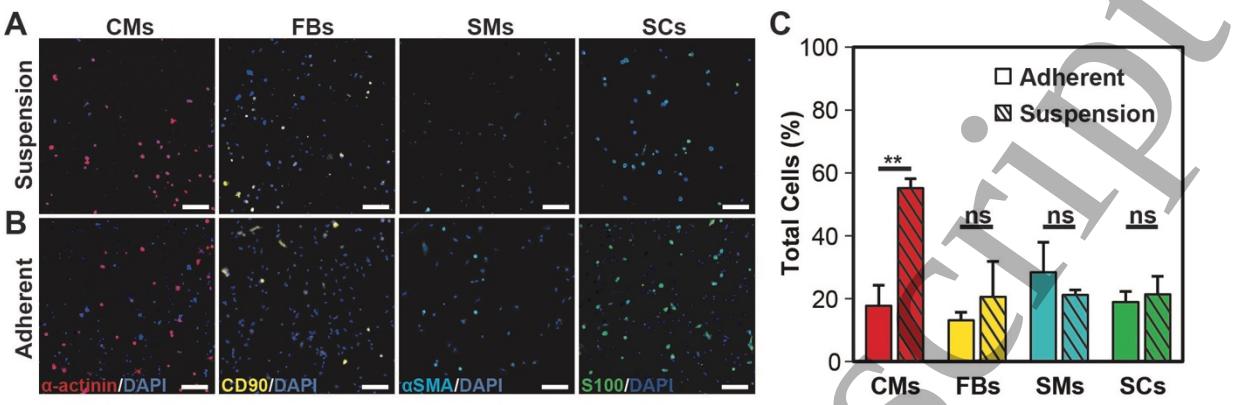

Figure 4. Immunofluorescent quantification of cardiac cellular composition. (A) Representative suspension and **(B)** adherent cultures grown on fibronectin coated cover slides for 12-18h post tissue dissociation. Cells were stained for markers for cardiomyocytes, sarcomeric alpha-actinin (red), fibroblast, CD90 (yellow), smooth muscle cells, alpha smooth muscle actin (cyan), Schwann cells, S100 (green) and cell nuclei, DAPI (blue). (C) Quantification of immunofluorescent images show that the suspension culture contains an enriched population of cardiomyocytes, with no statistical differences been other cell populations examined. (** $p < 0.05$, ns: not significant $p > 0.05$)

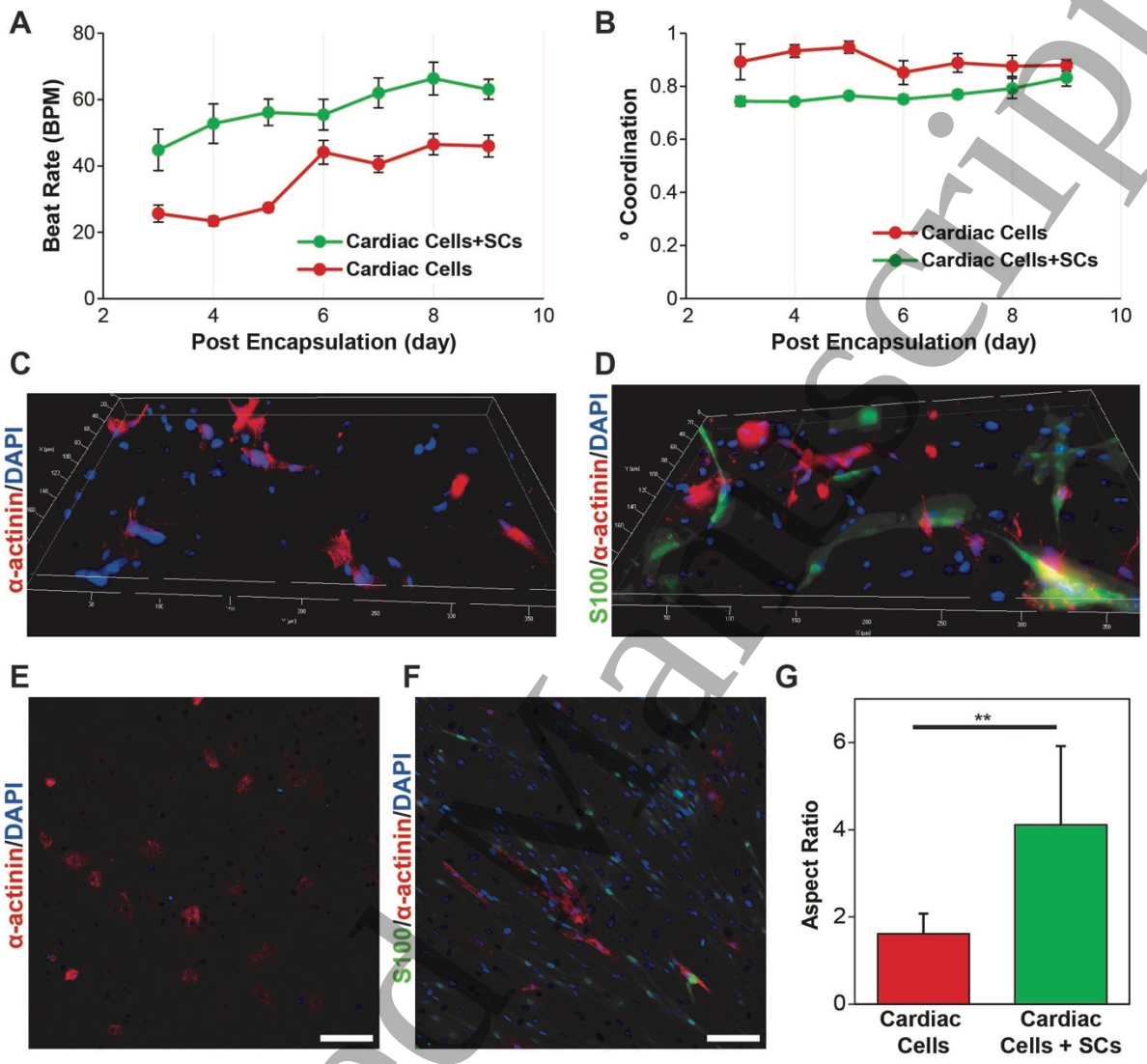

Figure 5. Role of SCs in the 2D and 3D cardiac cell cultures. (A) Quantification of BPM and **(B)** DoC for 3D μTissues over time showing that the inclusions of SCs leads to an increase and beat rate and decrease in coordinated contractions. **(C)** Representative immunofluorescent images of cardiac cells culture without and **(D)** with the inclusion of exogenous SCs encapsulated in 3D μTissues. **(E)** Representative immunofluorescent images of cardiac cells culture without and **(F)** with the inclusion of exogenous SCs in 2D (scale = 100 μm) and **(G)** CM aspect ratio quantification (** $p < 0.05$).

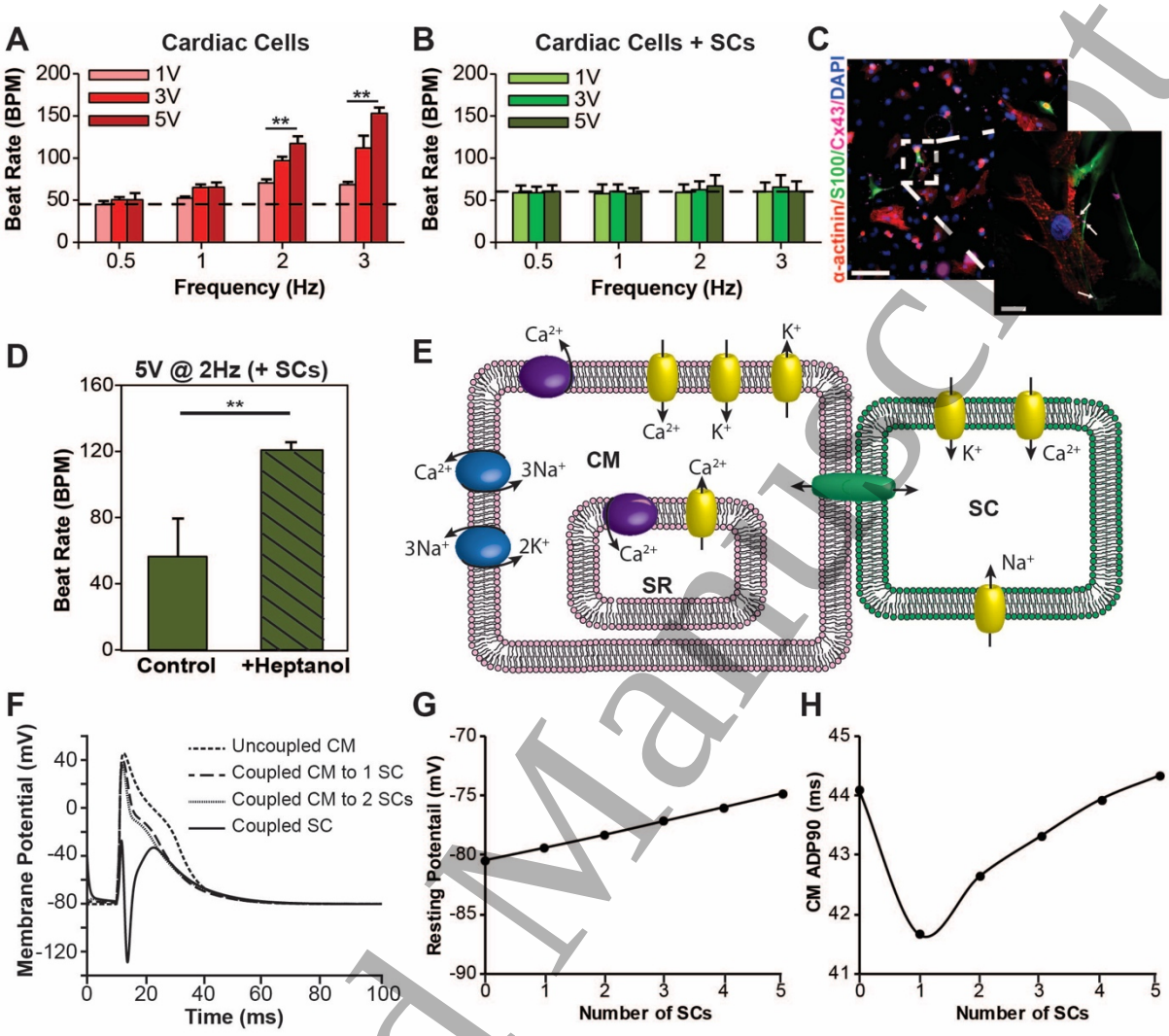

7.2 inch wide
scale 100um, 10um insert

Figure 6. External electrical pacing of 3D μTissues and computational modeling on CM-SC coupling. (A) Cardiomyocyte response to electrical stimuli at 0.5, 1, 2, and 3 Hz with increasing voltages from 1V to 3V to 5V shows cardiac μTissues can be paced (** $p < 0.05$), but **(B)** the inclusion of SCs prevents this electrical pacing (dashed line shows the average beat rate prior to electrical stimulation). **(C)** Representative immunofluorescent image showing the presence of connexin43 (Cx43) junctions (purple) between CMs (red) and SCs (green) (scale = 100 μm, inlay scale = 10 μm). White arrows indicate Cx43 positive staining at the interface of SCs and CMs. **(D)** Electrical pacing at 2Hz and 5V of individual CMs with exogenous SCs following heptanol treatment to block CM-SC coupling (** $p < 0.05$). These data represent CM beating from the same user identified cells before and after heptanol blocking (n = 5). **(E)** Schematic of a Hodgkin-Huxley model for CM-SC coupling. **(F)** Computational model of CM depolarization for one CM coupled to increasing numbers of SCs overplayed with a coupled SC membrane potential. **(G)** Changes in CM membrane potential and (H) APD90 with increased SC coupling.